Check for updates

Direct observation of geometric and sliding ferroelectricity in an amphidynamic crystal

Le-Ping Miao [1,2,3,6], Ning Ding [4,6], Na Wang [2,6], Chao Shi[2], Heng-Yun Ye [2], Linglong Li[4], Ye-Feng Yao [5], Shuai Dong [4]✉ and Yi Zhang [1,2,3]✉

Sliding ferroelectricity is a recently observed polarity existing in two-dimensional materials. However, due to the weak polarization and poor electrical insulation in these materials, existing experimental evidences are indirect and mostly based on nanoscale transport properties or piezoresponse force microscopy. We report the direct observation of sliding ferroelectricity, using a high-quality amphidynamic single crystal (15-crown-5)Cd_3Cl_6, which possesses a large bandgap and so allows direct measurement of polarization–electric field hysteresis. This coordination polymer is a van der Waals material, which is composed of inorganic stators and organic rotators as determined by X-ray diffraction and NMR characterization. From density functional theory calculations, we find that after freezing the rotators, an electric dipole is generated in each layer driven by the geometric mechanism, while a comparable ferroelectric polarization originates from the interlayer sliding. The net polarization of these two components can be directly measured and manipulated. Our finding provides insight into low-dimensional ferroelectrics, especially control of the synchronous dynamics of rotating molecules and sliding layers in solids.

Ferroelectrics are important smart materials that can facilitate conversions among electric, mechanical, thermal and optical signals. The most commercially popular ferroelectrics are three-dimensional (3D) inorganic crystals, such as $Pb(Zr_{1-x}Ti_x)O_3$ and $BaTiO_3$. In the quest for energy savings, greater integration and more flexibility, unconventional ferroelectrics are becoming highly attractive for a range of applications. For example, two-dimensional (2D) ferroelectrics are rapidly growing as an emerging branch[1–3], with several experimentally confirmed materials, such as SnTe monolayer[4], $CuInP_2S_6$ few-layers[5] and α-In_2Se_3 nanoflakes[6], and more predicted. In these materials, ferroelectricity can persist to the atomic level, making them superior to conventional 3D perovskites. Furthermore, exotic effects, such as giant negative piezoelectricity and sliding ferroelectricity, have been revealed in these systems[7,8].

Sliding ferroelectricity is a unique type of polarity that exists only in van der Waals (vdW) materials. Concretely, the stacking mode of vdW layers breaks the inversion symmetry, generating out-of-plane polarizations. Soon after the theoretical prediction of sliding ferroelectricity by Wu et al.[9], subsequent experiments found evidences of this polarity in WTe_2 bilayer/few-layer/flakes[10–12] and bilayer hexagonal BN[13,14]/1T′-ReS_2 (ref. [15])/R-MX_2 (M=Mo/W, X=S/Se)[16]. In addition, this sliding concept has been generalized to broader scopes, such as moiré ferroelectricity[8] and intralayer sliding[17]. Despite these achievements, existing experimental evidences are indirect (as summarized in Supplementary Table 1). In fact, many of these materials are semiconductors or even semi-metals, making the standard electrical measurements of ferroelectricity challenging. Alternatively, their ferroelectric properties were mostly characterized by the transport behaviours of nanodevices or piezoresponse force microscopy (PFM), with inevitable interference from leakage currents and environments. For example, the coercive

electric fields in transport measurements were high (of the order of $0.1\,V\,nm^{-1}$)[10,12], instead of the expected small value according to the sliding mechanism. Large coercivities and serious leakage will corrode the technical value of ferroelectrics.

Another interesting branch of polar materials is the family of molecular ferroelectrics[18,19]. In most of these materials, the polarity is caused by dipolar molecules, for example, pyridinium[20], benzylammonium[21], diisopropylammonium[22], pyrrolidinium[23] and cyclohexylammonium[24]. These dipolar molecules are dynamically disordered at high temperatures and ordered below their critical temperatures (T_C), leading to the alignment of dipoles and spontaneous polarizations. The ferroelectricity in a series of plastic molecular ferroelectrics, including molecular perovskite ferroelectrics, belongs to this type[25–27]. In addition, various non-dipolar dynamic molecules, such as crown-ethers and molecular gyroscopes, also exist. In a few crown-ether-based ferroelectrics, such as $[(C_7H_{10}NO)(18\text{-crown-6})][BF_4]$, $[(C_7H_{10}NO)(18\text{-crown-6})][ReO_4]$ and (m-FAni)-(Dibenzo[18]crown-6)$[Ni(dmit)_2]_{10}$ (m-FAni=m-fluoroanilinium; $dmit^{2-}$= 2-thioxo-1,3-dithiole-4,5-dithiolate)[28–30], ferroelectricity is ascribed to the alignment of rotating p-methoxyanilinium and m-fluoroanilinium, with the crown-ethers acting as stators. Compared with dipolar molecules, these non-dipolar dynamic molecules have been relatively ignored, and thus their ferroelectricity remains not fully understood.

In this work, the ferroelectricity in an amphidynamic vdW crystal coordination polymer (15-crown-5)Cd_3Cl_6 (CCC)[31] is unambiguously confirmed. Interestingly, the ferroelectricity of CCC has two sources. The first contribution comes from individual layers, whose dipoles are driven by the geometric frustration of oxygen ions once the rotational dynamics of crown-ethers are frozen. The second contribution is generated by interlayer sliding, which is the dominant

[1]Institute for Science and Applications of Molecular Ferroelectrics, Key Laboratory of the Ministry of Education for Advanced Catalysis Materials, Zhejiang Normal University, Jinhua, China. [2]Chaotic Matter Science Research Center, Department of Materials, Metallurgy and Chemistry & Jiangxi Provincial Key Laboratory of Functional Molecular Materials Chemistry, Jiangxi University of Science and Technology, Ganzhou, China. [3]Jiangsu Key Laboratory for Science and Applications of Molecular Ferroelectrics, Southeast University, Nanjing, China. [4]School of Physics, Southeast University, Nanjing, China. [5]Shanghai Key Laboratory of Magnetic Resonance, School of Physics and Electronic Science, East China Normal University, Shanghai, China. [6]These authors contributed equally: Le-Ping Miao, Ning Ding, Na Wang. ✉e-mail: sdong@seu.edu.cn; yizhang1980@seu.edu.cn
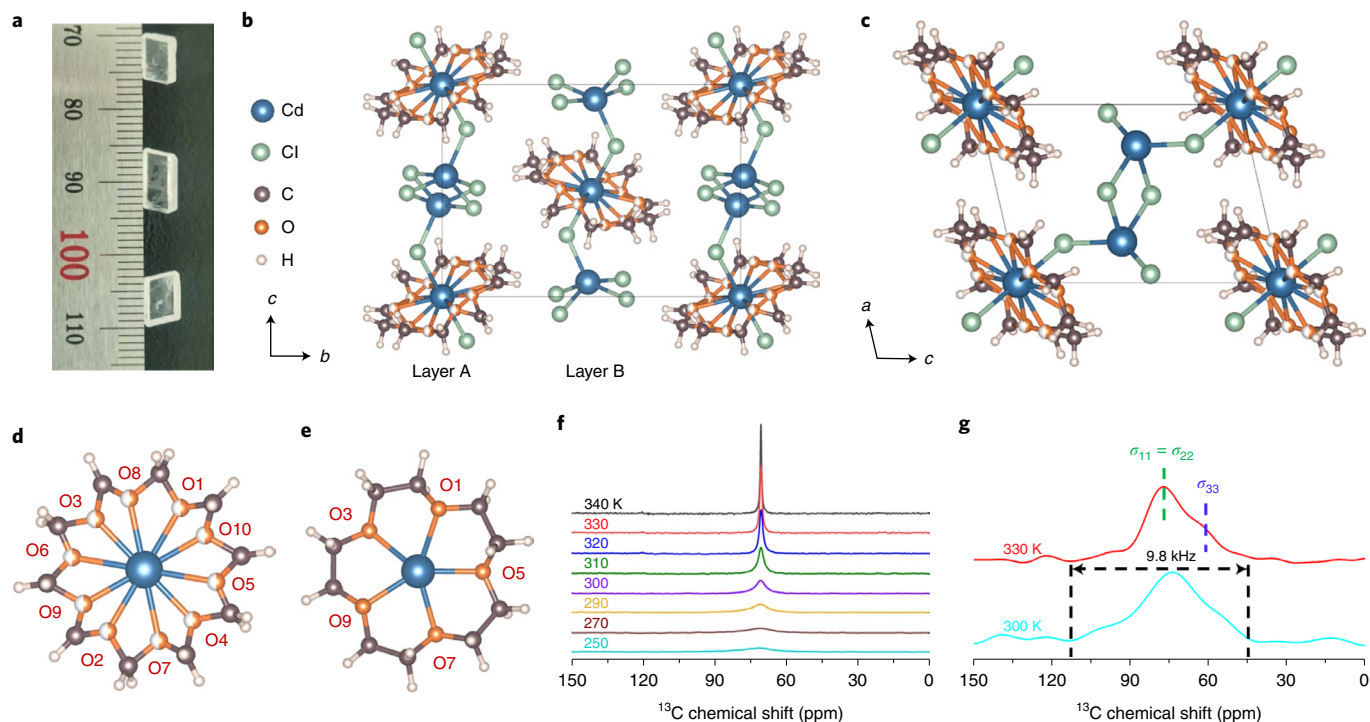
Fig. 1 | Structure of CCC. a, Image of single crystals. **b,c**, Schematic of the atomic structure of CCC in the HTP: side view (**b**), with the vdW stacking along the b axis; and top view of each vdW layer (**c**). **d,e**, Top views of a crown-ether in the HTP (**d**) and LTP (**e**). **f**, Temperature-dependent solid-state ^{13}C NMR spectra. These spectra were acquired by using a single-pulse excitation pulse sequence with a recycle delay of 2 s. **g**, ^{13}C CSA patterns at 300 K (below T_C) and 330 K (above T_C).

component of the overall polarization. These two components are positively superposed, going beyond established scenarios. Most importantly, directly proving sliding ferroelectricity in this highly insulating crystal extends sliding ferroelectricity to broader scopes and reduces the technical difficulties of manipulating this property.

Proof of amphidynamic properties of CCC crystal

Colourless and transparent rod-like single crystals of CCC in size of $3 \times 3 \times 8$ mm^3 (Fig. 1a and Supplementary Fig. 1) were grown by slow evaporation of a clear methanol solution containing stoichiometric amounts of CdCl$_2$ and 15-crown-5 at room temperature. Phase purity was confirmed by powder X-ray diffraction and infrared radiation analysis (Supplementary Figs. 2 and 3).

Based on differential scanning calorimetry analysis, CCC undergoes a phase transition at $T_C = 320$ K (Supplementary Fig. 4). Its crystal structures were determined by single-crystal X-ray diffraction at 253–343 K (Supplementary Note 1 and Supplementary Table 2). The high-temperature phase (HTP) is centrosymmetric with space group $P2_1/n$, while the symmetry of the low-temperature phase (LTP) is lowered to space group $P2_1$. Despite this difference, the crystal frameworks of both phases are similar. As shown in Fig. 1b,c, the unit cell (u.c.) of CCC consists of two layers (A and B) of adducts stacked along the b axis, and its structural unit can be described as a molecular pinwheel, where the crown-ether acts as the rotator.

CCC contains cadmium ions in two different chemical environments. The first kind of cadmium is surrounded by five chloride ions, forming a tetragonal pyramid. Neighbouring pyramids are edge-shared, forming 1D chains. The second kind of cadmium is located at the centre of 15-crown-5, coordinated by five equatorial oxygen ions and two axial chloride ions, forming a pentagonal bipyramid. The bipyramids link the chains into layers by sharing vertices with tetragonal pyramids. These layers are electrically

neutral and packed by vdW forces with an interlayer distance of 7.305(3) Å at 343 K (Supplementary Fig. 5).

In the HTP, the second kind of cadmium ion is located at the inversion centre (Fig. 1d). The model of 15-crown-5 determined from the Fourier difference map has five oxygen atoms distributed over ten sites and ten carbon atoms showing obvious larger thermal ellipsoids (Supplementary Fig. 6). This evidence initially reveals the rotation of 15-crown-5 in the HTP, which are frozen to fixed positions in the LTP (Fig. 1e).

To reveal the mechanical movement of the crown-ether, solid-state NMR spectroscopy is employed to probe the molecular motions in the frequency range from Hz to MHz. The motionally modulated ^{13}C isotropic signal is shown in Fig. 1f. Only one signal centred at 70.7 ppm is observed, which can be assigned to the CH$_2$ groups of crown-ether. At 250 K, the signal shows a large width with a half-width of 1,250 Hz, which becomes narrower and narrower upon heating. At 340 K, the signal half-width is reduced to only 70 Hz. This signal-narrowing phenomenon indicates the gradually increasing motions of crown-ether with increasing temperature[32,33].

The ^{13}C chemical shift anisotropy (CSA) signals above and below T_C are compared in Fig. 1g. At 300 K, the ^{13}C CSA pattern shows a complex asymmetric tensorial lineshape, implying very restricted mobility of the crown-ether. In contrast, its pattern at 330 K shows the typical features of an axially symmetric tensor with three principle values $\sigma_{11} = \sigma_{22} \neq \sigma_{33}$, indicating that the crown-ether undergoes a restricted anisotropic motion close to an axial rotation[34]. In addition, molecular motions with correlation times in the spectral time scale can cause the obvious lineshape perturbation[35,36]. The frequency ranges change from 9.8 kHz at 300 K to 3 kHz at 330 K, accompanied by a distinct change in the pattern lineshape. To produce such a lineshape perturbation, the frequency of molecular motion must be much higher than 9.8 kHz. Thus, the correlation
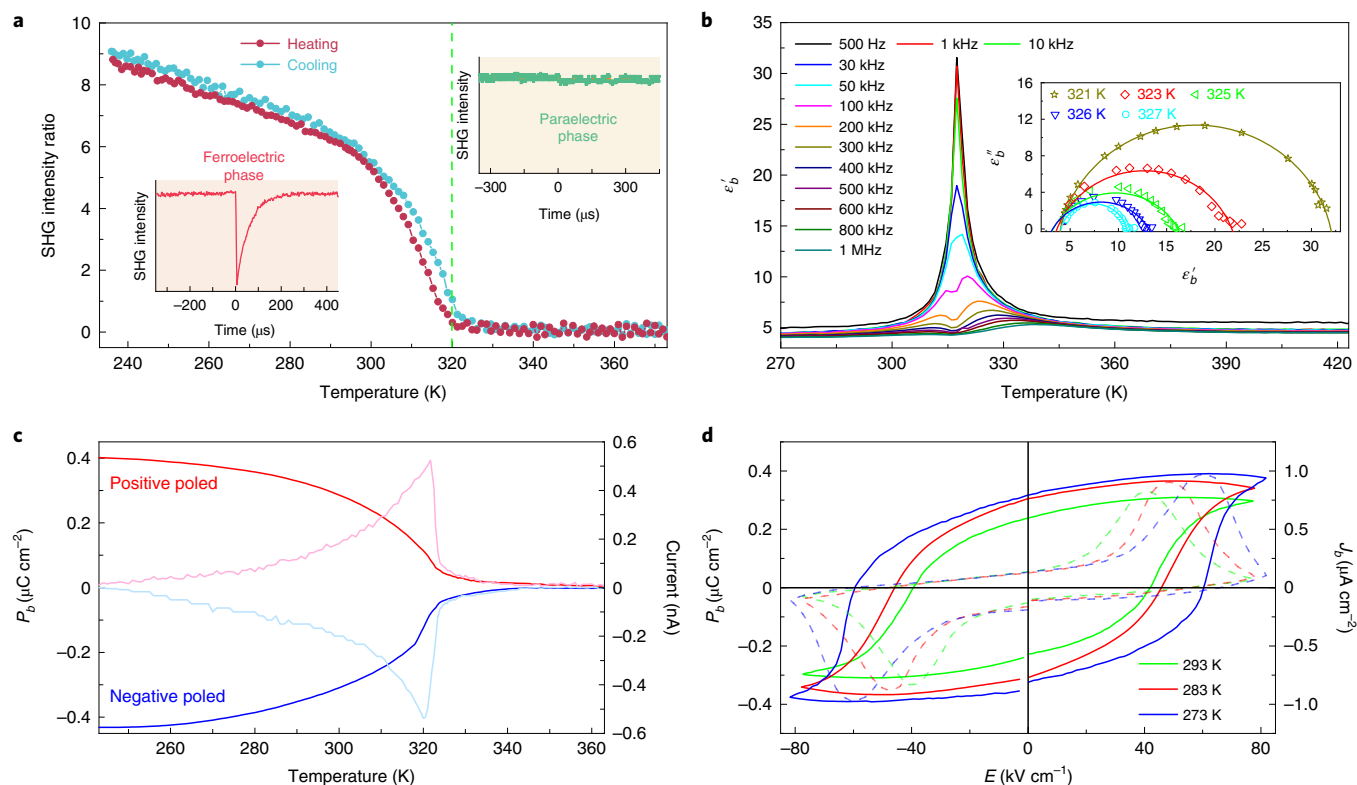
Fig. 2 | Characterization of ferroelectricity. a, The SHG intensity of CCC as a function of temperature in powder samples. The SHG intensity of quartz at room temperature is taken as the unit. Inset: comparison of SHG signals above and below T_C. **b-d**, Electrical characterizations measured along the b axis. **b**, The real part of the dielectric constant (ε'_b) at different frequencies. Inset: the relationship between ε'_b and ε''_b at temperatures slightly higher than T_C, showing typical Cole–Cole diagrams. **c**, Pyroelectric current (light curves) and integrated polarization (dark curves) showing the emergence of polarization below T_C. **d**, The J–E (broken) and P–E (solid) curves showing typical ferroelectric hysteresis loops.

time of molecular motions should be of the order of (sub)microseconds, consistent with the following dielectric behaviour.

In short, CCC is an amphidynamic crystal, with inorganic CdCl$_2$ chains as the stators and organic crown-ethers as the rotators above T_C.

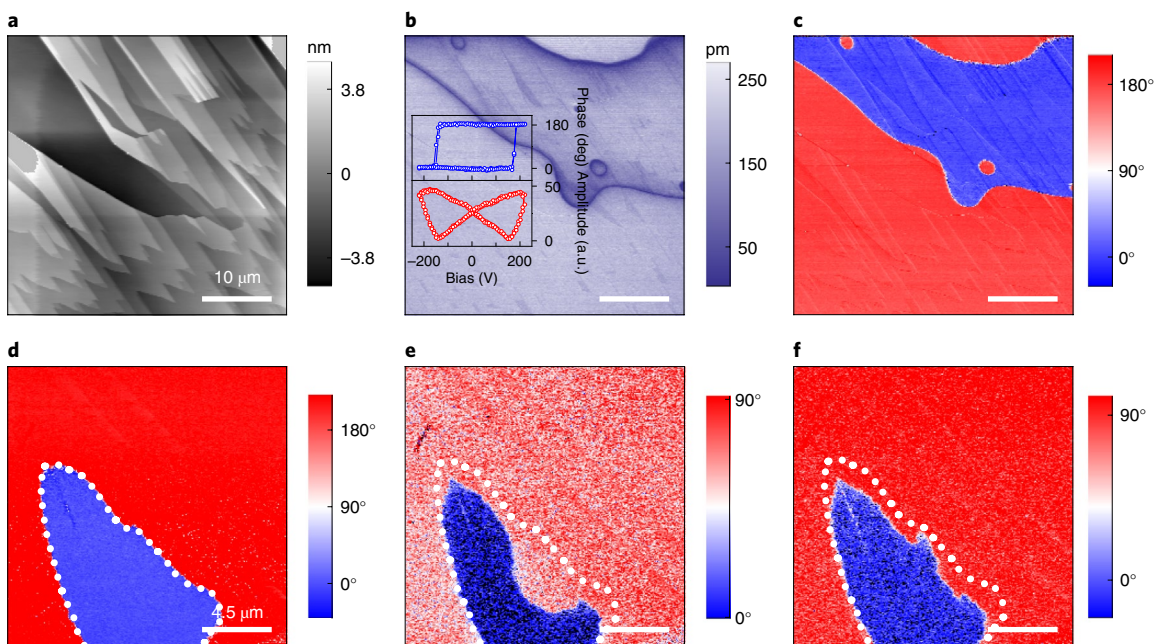## Characterization of ferroelectricity

According to above structural analysis, the order–disorder transition of crown-ethers induces a non-polar–polar transition of the CCC crystal, which can be characterized by the second harmonic generation (SHG) measurement on powder samples[37]. As expected, the SHG signal appears just below $T_C = 320$ K, and its intensity increases gradually upon cooling (Fig. 2a). At room temperature, its intensity is six times that of quartz. More information about SHG measurements and comparisons to other materials can be found in Supplementary Note 2, Supplementary Figs. 7 and 8, and Supplementary Table 3.

In addition, frequency-dependent dielectric curves are measured as a function of temperature to further verify the polarity of CCC[38]. As shown in Fig. 2b and Supplementary Fig. 9a,b, the dielectric constant along the b axis (ε'_b) is larger than those along the a and c axes (ε'_a and ε'_c), especially near T_C. This dielectric anisotropy agrees with CCC's space group $P2_1$, which allows spontaneous polarity only along the b axis. This dielectric anomaly is obvious over a wide frequency range of 500 Hz–1 MHz. For low frequencies, its real part ε'_b peaks at T_C (for example, ~30 at 1 kHz, six times of the room-temperature one), and its temperature dependence is typical of the continuous phase transition. For higher frequencies, ε'_b shows two broad maxima below and above T_C. The temperature dependence of its imaginary part ε''_b reveals a sharp maximum, the value

of which decreases with measurement frequency (Supplementary Fig. 9c). The spectra are similar to those observed for diglycine nitrate and Ca$_2$Sr(C$_2$H$_5$CO$_2$)$_6$ (ref. [39]) and exhibit a phenomenon known as dielectric critical slowing down, which is a characteristic of ferroelectrics that undergo order–disorder-type continuous phase transitions.

To derive more information, the Cole–Cole diagrams were analysed at five different temperatures slightly above T_C (Fig. 2b, insert). All these fitted plots are close to semicircles as expected for the ideal Debye relaxation model in which the dipoles are almost non-interacting. As summarized in Supplementary Table 4, the fitted Debye relaxation times are close to zero, indicating that the distribution of relaxation times is very narrow and the observed dielectric relaxation processes are monodispersive Debye relaxations. The relaxation time ranges from 4.82×10^{-6} s to 7.54×10^{-7} s in the temperature range from 321 to 327 K.

To confirm the ferroelectricity of CCC, it is necessary to prove the existence of an electrically switchable polarization below T_C. Our measurement indeed shows a continuous curve of pyroelectric current below T_C (peaking at T_C), the sign of which can be switched by the poling field (Fig. 2c). These pyroelectric behaviours strongly support its ferroelectricity below T_C. Furthermore, a polarization–electric field (P–E) hysteresis loop is the most decisive evidence of ferroelectricity. To obtain the P–E loops, the current–field (J–E) curves are measured under different temperatures (Fig. 2d). There are two peaks due to charge displacement, indicating two stable states with opposite polarity. Variable-temperature P–E hysteresis loops are obtained via current integration (Fig. 2d). As temperature decreases from 293 to 273 K, the coercive field increases from 40 to 60 kV cm^{-1}. The saturated polarization (P_S) are in the range

Fig. 3 | PFM characterization and manipulation of ferroelectric domains. a–c, Topology image of the crystal plane (010) of CCC (**a**) and the corresponding vertical PFM amplitude (**b**) and phase images (**c**). Inset of **b**: phase–voltage hysteresis loop and amplitude–voltage butterfly loop. **d–f**, The electrical switching of the ferroelectric domain: pristine (**d**), after applying a negative bias voltage (**e**) and after applying a positive bias voltage (**f**). The voltage of ±220 V is applied on the central area for 20 s. Scale bars: **a–c**, 10 μm; **d–f**, 4.5 μm.

0.3–0.4 μC cm^{-2} at 293–273 K, consistent with above pyroelectric values (Fig. 2c). With decreasing temperature, P_S becomes larger, in qualitative agreement with the increasing SHG signal intensity at low temperatures.

The ferroelectric domain structure is another essential element of ferroelectricity and can be determined by PFM. Figure 3a shows the topography of the (010) surface of the CCC single crystal. Domain textures from the amplitude and phase images in vertical PFM can be clearly seen in Fig. 3b,c. In contrast, in lateral PFM, very weak domain textures (which have the same shape as observed by vertical PFM) of the amplitude and phase images are observed (Supplementary Fig. 10a–c). These findings provide evidence for a strong vertical piezoresponse and a negligible lateral piezoresponse, implying that the polarization of CCC is only along the b axis.

To further reveal the switchable ferroelectricity of CCC, we recorded the vertical PFM switch spectroscopy loop, which indicates the effect of the phase and the amplitude signal on the DC tip bias in the same crystal sample through the measurement of point-wise polarization (Fig. 3b, inset). We also demonstrated the switching of ferroelectric domain in the homogeneous PFM amplitude and phase signal area (Fig. 3d–f and Supplementary Fig. 10d–f). The ferroelectric domain can be reversed and switched back by applying bias voltages. Achieving completing reversal of the domain confirms the ferroelectricity of CCC.

Geometric ferroelectricity

The above experimental evidences support an association between ferroelectricity and the disorder–order transition in crown-ethers. However, the symmetry-breaking mechanism in CCC differs from that in most previously studied amphidynamic crystals: here, the crown-ethers act as rotators rather than as stators as has been observed in many other molecules where the attached asymmetric groups rotate[28–30].

The first mechanism involved here can be termed geometric ferroelectricity. In the HTP, the 10 oxygen sites (and 10 carbon, 20 hydrogen and 2 chloride ions) in each crown-ether have inversion

symmetry with respect to the central cadmium ion. In particular, the O1–Cd–O2 bond angle is 180°, and the Cd-O1 and Cd-O2 bond lengths are equivalent (Fig. 1d). In the LTP, the five oxygen ions tend to keep away from each other due to Coulombic repulsion, that is, to occupy the odd- or even-index sites (Fig. 1e). The inversion symmetry is then naturally broken for each crown-ether, which further leads to stereo distortions of all ions in the crown-ether.

As illustrated in Fig. 4a, all oxygen ions deviate from the crown-ether plane more or less (to keep away from each other), mainly fluctuating in the −↑−↓− pattern (similar to the spin order in antiferromagnets). Meanwhile, the peripheral hydrogen ions fluctuate correspondingly in the −↓−↓−↑−↑− pattern. The odd number of oxygen ions in each crown-ether frustrates this mode within a period, creating a soliton in each crown-ether, together with hydrogen ions on the peripheral side. The two apical chloride ions of the crown-ether are also slightly influenced by the polar crown-ether, with staggered lengths of Cd–Cl bonds (slightly longer and shorter) and bending of the Cl–Cd–Cl bond angle to ~177.4° (Supplementary Fig. 11). This mechanism is similar to the ferroelectricity in hexagonal manganites/ferrites RMnO$_3$/RFeO$_3$ (R = rare earth or Y), where the displacements of R ions due to structural trimerization are frustrated due to the triangular geometry[40].

Thus, the crown-ether in the LTP can generate a dipole for each individual layer, which can be expressed as (p_a, p_b, p_c) for layer A and $(-p_a, p_b, -p_c)$ for layer B. This asymmetric (symmetric) relationship of the ac component (b component) between two layers are guaranteed by the $P2_1$ symmetry, which has a two-fold screw axis and allows a net polarization only along the b axis. The existence of dipoles in individual layers and the relationship between layers can be confirmed using density functional theory (DFT) calculations (Supplementary Note 3), as summarized in Table 1 and illustrated in Fig. 4b.

Sliding ferroelectricity

Although the geometric mechanism can qualitatively explain its polarization along the b axis, the dipole of a bulk u.c. (0.263 eÅ) is
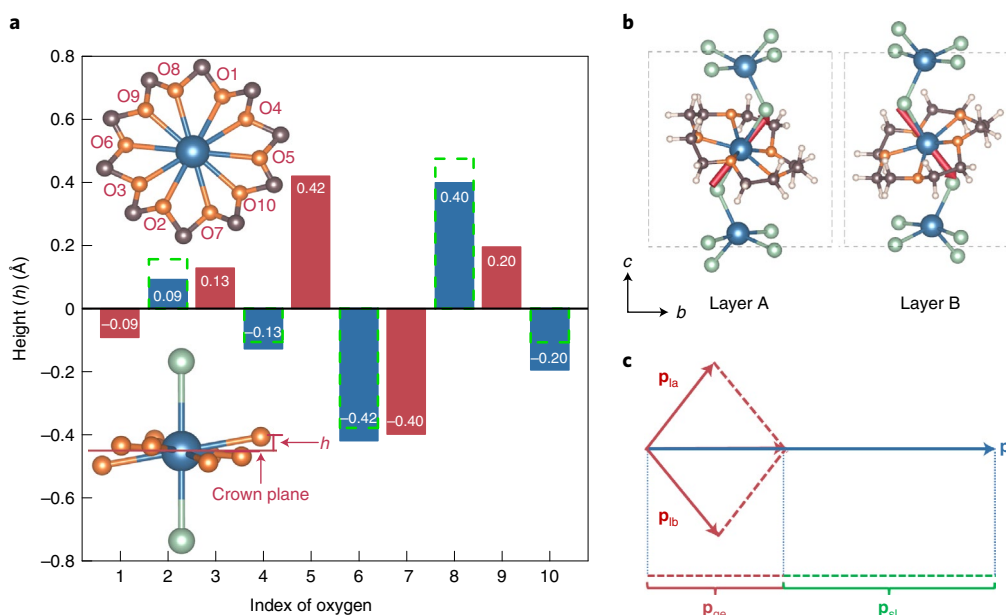
Fig. 4 | Schematic of geometric ferroelectricity. a, The height distribution of oxygen ions within a crown-ether relative to the crown-ether plane, according to the experimental structures. Inset: the definitions of index (upper) and height (lower). Solid bars with values: ten sites in the HTP; broken bars: five sites in the LTP. Odd and even bars are distinguished by colours. In the HTP, antisymmetry exists between odd-index and even-index sites, which is broken in the LTP since only odd-index (or even-index) sites are occupied. A soliton of the $-\uparrow-\downarrow-$ fluctuation is inevitable, which generates a dipole together with the peripheral carbon and hydrogen ions. **b**, The isolated layers A and B, rigidly extracted from the optimized bulk in the ferroelectric state. Their corresponding dipole vectors ($\mathbf{p}_{la}$ and $\mathbf{p}_{lb}$) are indicated by arrows. **c**, The superposition of $\mathbf{p}_{la}$ and $\mathbf{p}_{lb}$ leads to a net geometric dipole $\mathbf{p}_{ge}$ along the b axis, but it is smaller than the total dipole $\mathbf{p}$ of a bulk u.c. The surplus part is attributed to the sliding ferroelectric dipole, that is, $\mathbf{p}_{sl}$.

Table 1 | DFT partition of contributions from geometric and sliding components

	Dipole along (x, y, z)	Dipole along (a, b, c)
Isolated layer A	$\mathbf{p}_{la} = (-0.085, 0.056, 0.270)$	$\mathbf{p}_{la} = (-0.0193, 0.056, 0.278)$
Isolated layer B	$\mathbf{p}_{lb} = (0.085, 0.056, -0.270)$	$\mathbf{p}_{lb} = (0.0193, 0.056, -0.278)$
Isolated layers A + B	$\mathbf{p}_{ge} = \mathbf{p}_{la} + \mathbf{p}_{lb} = (0, 0.112, 0)$	
Bulk (A + B stacking)	$\mathbf{p} = \mathbf{p}_{ge} + \mathbf{p}_{sl} = (0, 0.263, 0)$	

Dipoles for individual layers and bulk u.c. are shown in units of e Å. The coordinate (x, y, z) is orthorhombic. The crystalline axes are $a||x$, $b||y$, but c is along (-0.236, 0, 0.972). $\mathbf{p}_{la}/\mathbf{p}_{lb}$, geometric dipole of a single isolated layer A/B; $\mathbf{p}_{ge}$, net geometric dipole within one u.c.; $\mathbf{p}_{sl}$, sliding dipole of bulk u.c.; $\mathbf{p}$, total dipole of bulk u.c.

obviously larger than the direct sum of two isolated layers (0.112 eÅ) (Fig. 4c and Table 1), much beyond the allowable precision. Thus, another contribution must exist that is non-negligible (in fact dominant) since its contribution amounts to 57.4% of total.

This additional ferroelectric origin is from the vdW interlayer sliding. Although the experimental measurements of ferroelectricity cannot directly distinguish the individual contributions geometric and sliding ferroelectricity, the existence of sliding ferroelectricity in CCC can be unambiguously demonstrated by monitoring ion positions, determined from the single-crystal X-ray diffraction measurements and DFT structural relaxation. Analysis of the HTP and LTP structures of CCC indeed reveals the existence of interlayer sliding (Fig. 5a). Using the cadmium ions in crown-ethers as the indication, the relative sliding distance in the ac plane is 0.30 Å according to the experimental HTP and LTP structures, which is

confirmed in our DFT calculation (0.62 Å between the $\pm P$ ferroelectric states). This displacement is large enough to be precisely captured in DFT calculations. For reference, the DFT displacement of Mn in BaMnO$_3$ is only 0.038 Å (ref. [41]).

The sliding indeed reduces the energy to the minimum (Fig. 5b), and further sliding beyond this optimal level is not energy favourable. The polarization contribution due to interlayer sliding is perpendicular to the vdW layers, as expected for all sliding ferroelectrics, which superposes on the aforementioned geometric one along the b axis (Fig. 5c). Naturally, its polarization is proportional to the sliding distance.

Unlike previous sliding ferroelectrics, here non-zero ferroelectric polarizations exist in the so-called '0' states, partially arising from geometric dipoles. In addition, although Cd2 is not sliding in the '0' states, other ions can still slide in a non-rigid manner (Supplementary Fig. 12) and generate a sliding dipole. Thus, even in the '0' states, the net polarizations are comprised of both geometric and sliding sources. Furthermore, if the geometric contribution along the b axis is turned off in the DFT calculation, the interlayer sliding and corresponding polarization along the b axis also diminish to zero (Supplementary Note 3), implying the sliding dipole is probably secondary to the geometric one.

Discussion

Due to the coupling between the two components, sliding is unidirectional when the sign of the geometric polarization is fixed. This is reasonable because the existence of geometric ferroelectricity breaks the inversion symmetry. As a result, with a given geometric component, the energy profile as a function of sliding changes from a double-well to a single-well structure. The expected double-well energy profile can be restored by flipping the geometric and sliding components together, satisfying the requirement of ferroelectric switchability. This coupling effect is absent in previous sliding ferroelectrics but is similar to the hybrid improper ferroelectricity in
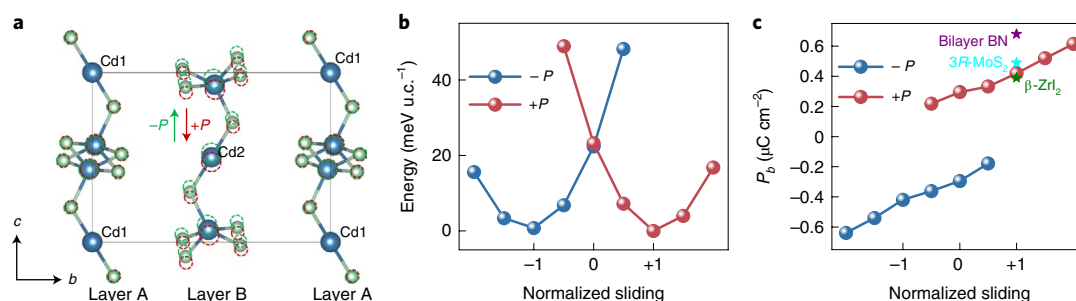
Fig. 5 | Schematic of sliding ferroelectricity. a, The ion displacements of $CdCl_2$ chains. Solid outlines, HTP; dashed outlines, LTP ($\pm P$). The organic parts are not shown for simplicity. All displacements are defined relative to Cd1. The arrows indicate the sliding directions, not the polarization directions. **b,c**, The sliding-dependent energy (**b**) and polarization (**c**). The signs of the geometric contribution are distinguished by colours. The interlayer sliding is characterized by the relative shift of Cd2, normalized to its optimized shift (see Supplementary Note 3 for more details). For comparison, the polarizations of other sliding ferroelectrics are shown as stars. The value of bilayer BN was determined experimentally[45], whereas the others were calculated by DFT[8].

$Ca_3Ti_2O_7$ and $Ca_3Mn_2O_7$ (refs. [42–44]), the polarization of which also depends on two coupled degrees of freedom.

Limited by the weak vdW interaction, the polarizations of sliding ferroelectrics may be naturally small (typically ~1 μC cm^{-2} or less)[8]. Inspired by this work, a promising direction for sliding ferroelectricity is to couple multiple ferroelectric sources in one material, which can strengthen the net polarization and provide more degrees of freedom for manipulation. For example, here the interlayer sliding can trigger the flipping of geometric polarization, and vice versa.

In addition, a noteworthy advantage of CCC is its highly insulating property, which can reduce the leakage current in ferroelectric measurements to a minimum. Direct ferroelectric measurements then become possible and reliable; these are difficult to achieve for semiconducting or semi-metallic sliding ferroelectrics. Indeed, our DFT calculation finds a large bandgap of ~4 eV (Supplementary Fig. 13), in agreement with the transparency and lack of colour of CCC. As a result, our work can provide direct characterizations of CCC's ferroelectricity, which is a decisive step for the study of sliding ferroelectricity.

Perspective

Our study unambiguously demonstrated that the ferroelectricity of CCC originates from both geometric and sliding mechanisms. Although a few molecular ferroelectrics have been developed in recent years, layered molecular ferroelectrics remain rare. Even in those few layered molecular ferroelectrics, spontaneous polarizations are simply induced by the alignment of discrete organic ammonium cations, leading to in-plane polarizations. Thus, our work is not simply a marginal extension of previous work on molecular ferroelectrics but describes a range of considerably more exotic ferroelectricity mechanisms. Both geometric and sliding ferroelectricity were previously reported only in pure inorganic materials. Our study extends these two kinds of polarity into the field of molecular ferroelectrics, enriching scientific knowledge of organic–inorganic hybrid systems and broadening the range of material candidates for future applications. Thus, the present work opens a door to explore more ferroelectric mechanisms and materials in organic–inorganic hybrid systems.

Online content

Any methods, additional references, Nature Research reporting summaries, source data, extended data, supplementary information, acknowledgements, peer review information; details of author contributions and competing interests; and statements of data and code availability are available at https://doi.org/10.1038/s41563-022-01322-1.

References

1. Qi, L., Ruan, S. & Zeng, Y. Review on recent developments in 2D ferroelectrics: theories and applications. *Adv. Mater.* **33**, 2005098 (2021).
2. Wu, M. Two-dimensional van der Waals ferroelectrics: scientific and technological opportunities. *ACS Nano* **15**, 9229–9237 (2021).
3. Guan, Z. et al. Recent progress in two-dimensional ferroelectric materials. *Adv. Electron. Mater.* **6**, 1900818 (2020).
4. Chang, K. et al. Discovery of robust in-plane ferroelectricity in atomic-thick SnTe. *Science* **353**, 274–278 (2016).
5. Liu, F. et al. Room-temperature ferroelectricity in $CuInP_2S_6$ ultrathin flakes. *Nat. Commun.* **7**, 12357 (2016).
6. Zhou, Y. et al. Out-of-plane piezoelectricity and ferroelectricity in layered α-In_2Se_3 Nano flakes. *Nano Lett.* **17**, 5508–5513 (2017).
7. You, L. et al. Origin of giant negative piezoelectricity in a layered van der Waals ferroelectric. *Sci. Adv.* **5**, eaav3780 (2019).
8. Wu, M. & Li, J. Sliding ferroelectricity in 2D van der Waals materials: related physics and future opportunities. *Proc. Natl Acad. Sci. USA* **118**, e2115703118 (2021).
9. Li, L. & Wu, M. Binary compound bilayer and multilayer with vertical polarizations: two-dimensional ferroelectrics, multiferroics, and nanogenerators. *ACS Nano* **11**, 6382–6388 (2017).
10. Fei, Z. et al. Ferroelectric switching of a two-dimensional metal. *Nature* **560**, 336–339 (2018).
11. Sharma, P. et al. A room-temperature ferroelectric semimetal. *Sci. Adv.* **5**, eaax5080 (2019).
12. Xiao, J. et al. Berry curvature memory through electrically driven stacking transitions. *Nat. Phys.* **16**, 1028–1034 (2020).
13. Yasuda, K., Wang, X., Watanabe, K., Taniguchi, T. & Jarillo-Herrero, P. Stacking-engineered ferroelectricity in bilayer boron nitride. *Science* **372**, 1458–1462 (2021).
14. Stern, M. V. et al. Interfacial ferroelectricity by van der Waals sliding. *Science* **372**, 1462–1466 (2021).
15. Wan, Y. et al. Room-temperature ferroelectricity in 1T′-ReS_2 multilayers. *Phys. Rev. Lett.* **128**, 067601 (2022).
16. Wang, X. et al. Interfacial ferroelectricity in rhombohedral-stacked bilayer transition metal dichalcogenides. *Nat. Nanotech.* https://doi.org/10.1038/s41565-021-01059-z (2022).
17. Wang, Z. et al. Ferroelectricity in strained Hf_2CF_2 monolayer. *Phys. Rev. Mater.* **5**, 074408 (2021).
18. Zhang, W. & Xiong, R.-G. Ferroelectric metal–organic frameworks. *Chem. Rev.* **112**, 1163–1195 (2012).
19. Horiuchi, S. & Tokura, Y. Organic ferroelectrics. *Nat. Mater.* **7**, 357–366 (2008).
20. Czarnecki, P., Nawrocik, W., Pajak, Z. & Wasicki, J. Ferroelectric properties of pyridinium tetrafluoroborate. *Phys. Rev. B* **49**, 1511–1512 (1994).
21. Liao, W. Q. et al. A lead-halide perovskite molecular ferroelectric semiconductor. *Nat. Commun.* **6**, 7338 (2015).
22. Fu, D. W. et al. Diisopropylammonium chloride: a ferroelectric organic salt with a high phase transition temperature and practical utilization level of spontaneous polarization. *Adv. Mater.* **23**, 5658–5662 (2011).
23. Zhang, Y. et al. Highly efficient red-light emission in an organic–inorganic hybrid ferroelectric: (pyrrolidinium)$MnCl_3$. *J. Am. Chem. Soc.* **137**, 4928–4931 (2015).
24. Ye, H. Y. et al. Bandgap engineering of lead-halide perovskite-type ferroelectrics. *Adv. Mater.* **28**, 2579–2586 (2016).
25. Harada, J. et al. Directionally tunable and mechanically deformable ferroelectric crystals from rotating polar globular ionic molecules. *Nat. Chem.* **8**, 946–952 (2016).

26. You, Y. M. et al. An organic-inorganic perovskite ferroelectric with large piezoelectric response. *Science* **357**, 306–309 (2017).

27. Ye, H. Y. et al. Metal-free three-dimensional perovskite ferroelectrics. *Science* **361**, 151–155 (2018).

28. Fu, D. W. et al. 4-Methoxyanilinium perrhenate 18-crown-6: A new ferroelectric with order originating in swinglike motion slowing down. *Phys. Rev. Lett.* **110**, 257601 (2013).

29. Fu, D. W. et al. Supramolecular bola-like ferroelectric: 4-methoxyanilinium tetrafluoroborate-18-crown-6. *J. Am. Chem. Soc.* **133**, 12780–12786 (2011).

30. Akutagawa, T. et al. Ferroelectricity and polarity control in solid-state flip-flop supramolecular rotators. *Nat. Mater.* **8**, 342–347 (2009).

31. Hazell, A., Hazell, R. G., Holm, M. F. & Krogh, L. Structures of the 3:1 adducts of cadmium(II) bromide and of cadmium(II) chloride with 15-crown-5 ether: structural changes induced by radiation. *Acta Crystallogr.* **47**, 234–239 (1991).

32. Fu, X. B. et al. Revealing structure and dynamics in host–guest supramolecular crystalline polymer electrolytes by solid-state NMR: applications to β-CD-polyether/Li⁺ crystal. *Polymer* **105**, 310–317 (2016).

33. Rothwell, W. P., Shen, W. X. & Lunsford, J. H. ³¹P Solid-state NMR of a chemisorbed phosphonium ion in HY zeolite: observation of ¹H-³¹P J coupling in the solid state. *J. Am. Chem. Soc.* **106**, 2452–2453 (1984).

34. Shi, C., Zhang, X., Cai, Y., Yao, Y.-F. & Zhang, W. A chemically triggered and thermally switched dielectric constant transition in a metal cyanide based crystal. *Angew. Chem.* **127**, 6304–6308 (2015).

35. Schmidt-Rohr, K. & Spiess, H. W. *Multidimensional Solid-state NMR and Polymers* (Academic Press, 1994).

36. Levitt, M. H. *Spin Dynamics: Basics of Nuclear Magnetic Resonance.* (John Wiley, 2001).

37. Kurtz, S. K. & Perry, T. T. A powder technique for the evaluation of nonlinear optical materials. *J. Appl. Phys.* **39**, 3798–3813 (1968).

38. Lines, M. E. & Glass., A. M. *Principles and Applications of Ferroelectrics and Related Materials* (Oxford University Press, 1977).

39. Czapla, Z. & Grigas, J. Microwave dielectric dispersion in diglycine nitrate. *Ferroelectrics* **100**, 187–194 (1989).

40. Van Aken, B. B., Palstra, T. T. M., Filippetti, A. & Spaldin, N. A. The origin of ferroelectricity in magnetoelectric YMnO₃. *Nat. Mater.* **3**, 164–170 (2004).

41. Rondinelli, J. M., Eidelson, A. S. & Spaldin, N. A. Non-d^0 Mn-driven ferroelectricity in antiferromagnetic BaMnO₃. *Phys. Rev. B* **79**, 205119 (2009).

42. Benedek, N. A. & Fennie, C. J. Hybrid improper ferroelectricity: a mechanism for controllable polarization–magnetization coupling. *Phys. Rev. Lett.* **106**, 107204 (2011).

43. Oh, Y. S., Luo, X., Huang, F.-T., Wang, Y.-Z. & Cheong, S.-W. Experimental demonstration of hybrid improper ferroelectricity and the presence of abundant charged walls in (Ca,Sr)₃Ti₂O₇. crystals. *Nat. Mater.* **14**, 407 (2015).

44. Liu, M. F. et al. Direct observation of ferroelectricity in Ca₃Mn₂O₇ and its prominent light absorption. *Appl. Phys. Lett.* **113**, 022902 (2018).

45. Ding, N. et al. Phase competition and negative piezoelectricity in interlayer-sliding ferroelectric ZrI₂. *Phys. Rev. Mater.* **5**, 084405 (2021).

Methods

Differential scanning calorimetry, SHG and X-ray diffraction measurements.
Differential scanning calorimetry measurements were performed on a Netzsch
214 Polyma calorimeter under a nitrogen atmosphere in aluminium crucibles
with a heating or cooling rate of $10\,K\,min^{-1}$. For SHG experiments, samples with
particle sizes of $75-150\,\mu m$ were used to measure the SHG intensity with a pumped
Nd:YAG laser (1064 nm, 1 Hz repetition rate), with the temperature varying from
220 to 380 K controlled by a precision temperature controller system (HCS302,
Instec Instruments). Variable-temperature X-ray diffraction analysis was carried
out using a Rigaku synergy diffractometer with Mo Kα radiation ($\lambda = 0.71073\,\text{Å}$).
Data collection, cell refinement and data reduction were performed using the
CrysAlisPro v.1.171.41.112a XtaLAB Synergy-R online system. The structures
were solved by the direct method and refined by the full-matrix method based on
F^2 using the OLEX2 and SHELXTL (2018) software package. All non-hydrogen
atoms were refined anisotropically, and the positions of all hydrogen atoms were
generated geometrically. The powder X-ray diffraction pattern (Supplementary
Figure 2) was refined using the GSAS Rietveld program[46]. The electron density
profile (Supplementary Fig. 6) was obtained from PLATON[47].

Dielectric, pyroelectric and ferroelectric measurements. For dielectric and
ferroelectric measurements, the samples were made with single crystals cut into
the form of thin plates (thickness, ~0.3–0.6 mm) perpendicular to the crystalline
a, *b* and *c* axes. The direction of the single crystal was determined with a Rigaku
OD synergy diffractometer (operating system: CrysAlisPro 1.171.41.112a). Silver
conduction paste deposited on the plate surfaces was used as the electrodes.
Complex dielectric permittivities were measured with a TH2828A impedance
analyser over the frequency range from 500 Hz to 1 MHz with an applied electric
field of 0.5 V. Pyroelectric property was measured with an electrometer/high
resistance meter (Keithley 6517B) with a heating rate of $10\,K\,min^{-1}$. *J–V* curves
were measured using the double-wave method, which can remove non-hysteresis
components in *P–E* loops[48]. Ferroelectric switching measurements were directly
carried out on the monocrystal by scanning probe microscopy through a
resonant-enhanced PFM (MFP-3D, Asylum Research) and conductive Pt/Ir-coated
silicon probes (EFM-50, Nanoworld).

Solid-state NMR experiments. The ^{13}C solid-state NMR experiments were
performed on a Bruker AVANCE III 400 WB spectrometer operating at
100.06 MHz for ^{13}C. A 4 mm double-resonance magic angle spinning probe
was used for the ^{13}C experiments. The temperature-dependent high-resolution
solid-state ^{13}C NMR spectra were acquired using the single-pulse excitation pulse
sequence with a recycle delay of 2 s. A 4 mm magic angle spinning probe was used
in the experiments, and the spinning speed was 10 kHz. The ^{13}C CSA patterns were
extracted from the 2D SUPER spectra[49].

DFT calculation. The first-principles DFT calculations were performed with
projector-augmented wave pseudopotentials as implemented in the Vienna
ab initio Simulation Package[50]. The Perdew–Burke–Ernzerhof parameterization
of the generalized gradient approximation was used for the exchange-correlation
functional[51]. The plane-wave cutoff energy was 550 eV. The *k*-point grids of
$5 \times 3 \times 3$ were adopted for both structural relaxation and static computation. To
describe the interlayer interaction, the vdW correction of the DFT-D3 method is
adopted[52], which leads to lattice constants closer to the experimental values than
obtained with other corrections. The convergent criterion for the energy was set
to $10^{-6}\,eV$, and the default criterion of the Hellman–Feynman force during the
structural relaxation was $<0.01\,eV\,\text{Å}^{-1}$ for all atoms. In addition, the polarization
was calculated using the standard Berry phase method[53,54]. More benchmarks of
DFT calculations can be found in Supplementary Note 3, Supplementary Fig. 14
and Supplementary Table 5.

Data availability

The experimental cif files can be found in CCDC (1875017-1875018 and
2160711-2160716). The experimental and DFT optimized structural files were
also uploaded as supplementary files. Source data for figures in main text and

supplemental information of this paper are available at https://figshare.com/
articles/dataset/Direct_observation_of_geometric_and_sliding_ferroelectricity_
in_an_amphidynamic_crystal/20102213. Other data supporting these findings are
available from the corresponding authors upon request. Source data are provided
with this paper.

References

46. Larson, A. C. & Von Dreele, R. B. *General Structure Analysis System (GSAS)*
    (Los Alamos National Laboratory Report LAUR 86-748, 1994).
47. Spek, A. L. *PLATON, A Multipurpose Crystallographic Tool* (Utrecht
    University, 2001); http://www.cryst.chem.uu.nl/platon/
48. Fukunaga, M. & Noda, Y. New technique for measuring ferroelectric and
    antiferroelectric hysteresis loops. *J. Phys. Soc. Jpn.* **77**, 64706 (2008).
49. Liu, S. F., Mao, J. D. & Schmidt-Rohr, K. A robust technique for
    two-dimensional separation of undistorted chemical-shift anisotropy powder
    patterns in magic-angle-spinning NMR. *J. Magn. Reson.* **155**, 15–28 (2002).
50. Kresse, G. & Furthmu, J. Efficient iterative schemes for ab initio total-energy
    calculations using a plane-wave basis set. *Phys. Rev. B* **54**, 11169–11186 (1996).
51. Perdew, J. P., Burke, K. & Ernzerhof, M. Generalized gradient approximation
    made simple. *Phys. Rev. Lett.* **77**, 3865–3868 (1996).
52. Grimme, S., Antony, J. & Ehrlich, S. A consistent and accurate ab initio
    parametrization of density functional dispersion correction (DFT-D) for the
    94 elements H–Pu. *J. Chem. Phys.* **132**, 154104 (2010).
53. Resta, R. Macroscopic polarization in crystalline dielectrics: the geometric
    phase approach. *Rev. Mod. Phys.* **66**, 899–915 (1994).
54. King-Smith, R. D. & Vanderbilt, D. Theory of polarization of crystalline
    solids. *Phys. Rev. B* **47**, 1651–1654 (1993).

Author contributions

Y.Z. and S.D. conceived the project. Y.Z. designed the experiments. S.D. proposed the
theoretical mechanisms. L.-P.M. prepared the samples and performed the DSC and SHG
measurements. N.W. contributed to PFM measurements. C.S. and H.-Y.Y. contributed
to single-crystal measurement and analysis. Y.-F.Y. performed the NMR measurement
and analysis. N.D. performed the DFT calculations guided by S.D. L.L. contributed to the
analysis of PFM. S.D. and Y.Z. wrote the manuscript, with inputs from all other authors.

Competing interests

The authors declare no competing interests.

Additional information

Supplementary information The online version contains supplementary material
available at https://doi.org/10.1038/s41563-022-01322-1.

Correspondence and requests for materials should be addressed to Shuai Dong
or Yi Zhang.

Peer review information *Nature Materials* thanks Sarah Guerin and the other,
anonymous, reviewer(s) for their contribution to the peer review of this work.

Reprints and permissions information is available at www.nature.com/reprints.